Wind and Structures, *Vol. 30, No. 4 (2020) 405-421*
DOI: https://doi.org/10.12989/was.2020.30.4.405

Probabilistic and spectral modelling of dynamic wind effects of quayside container cranes

Su Ning[a], Peng Shitao[b], Hong Ningning*,Wu Xiaotong[c] and Chen Yunyue[d]

Key Laboratory of Environmental Protection in Water Transport Engineering, Tianjin Research Institute for Water Transport Engineering, China Ministry of Transport, Tianjin, 300456, China

(Received January 29, 2019, Revised May 7, 2019, Accepted May 9, 2019)

Abstract. Quayside container cranes are important delivery machineries located in the most frontiers of container terminals, where strong wind attacks happen occasionally. Since the previous researches on quayside container cranes mainly focused on the mean wind load and static response characteristics, the fluctuating wind load and dynamic response characteristics require further investigations. In the present study, the aerodynamic wind loads on quayside container cranes were obtained from wind tunnel tests. The probabilistic and spectral models of the fluctuating aerodynamic loads were established. Then the joint probabilistic distributions of dynamic wind-induced responses were derived theoretically based on a series of Gaussian and independent assumption of resonant components. Finally, the results were validated by time domain analysis using wind tunnel data. It is concluded that the assumptions are acceptable. And the presented approach can estimate peak dynamic sliding force, overturning moments and leg uplifts of quayside container cranes effectively and efficiently.

Keywords: quayside container crane; probabilistic distribution; spectral model; wind tunnel tests; wind-induced response

1. Introduction

As a kind of important delivery machinery widely used in container terminals, quayside container cranes are usually located in the frontiers of quays and ports, which are directly subjected to strong winds. The wind-induced damage occasionally occurs to the quayside container cranes (McCarthy and Vazifdar 2004, McCarthy *et al*. 2007 and 2009), which were usually caused by wind-induced sliding and overturning. Especially, on June 13th 2018, five quayside container cranes in China Qingdao port were blown down (Fig. 1), which caused enormous losses. However, previous studies on the aerodynamics mainly focused on the mean wind load characteristics (Huang *et al*. 2007, Gu *et al*. 2008, Lee and Kang 2008, Kang and Lee 2008, Han and Han 2011). The accident indicated us that it is necessary to further study the fluctuating wind load and the dynamic wind-induced responses of quayside container cranes.

On the studies of wind load of quayside container cranes cranes, wind tunnel tests and CFD simulations were carried out in literatures (Huang *et al*. 2007, Gu *et al*. 2008, Lee and Kang 2008, Kang and Lee 2008, Sun *et al*. 2009, Han and Han 2011). These researches mainly focused on the mean wind load and static wind-induced responses. Sourav and Samit (2014) analyzed the stationary and non-stationary dynamic wind effect and vulnerability of quayside container cranes through stochastic simulation. However, the study was based on quasi-steady theory. The influences of the body-induced turbulence on the structure were not considered. Takahashi *et al*. (2016) analyzed the dynamic runaway characteristics of quayside container cranes subjected to a storm with a sudden change of mean wind speed, which lacks consideration of fluctuating component of wind load. However, the realistic quayside container cranes were located in coastal boundary layer, the turbulence induced aerodynamic fluctuating wind loads act as a background component in the dynamic wind-induced vibration, which would also cause significant dynamic resonant amplification as the structure become higher and

Fig. 1 Five quayside container cranes were blown down by a strong transient gusty wind (Qingdao Port 2018)

*Corresponding author, Ph. D.
E-mail: 15822850239@163.com
[a]Ph. D.
E-mail: souvenire@126.com
[b]Ph. D.
E-mail: pengshitao@126.com
[c]Ph. D.
E-mail: 635757797@qq.com
[d]Research Assistant
E-mail: yunyuechen123@126.com

Copyright © 2020 Techno-Press, Ltd.

ISSN: 1226-6116 (Print), 1598-6225 (Online)

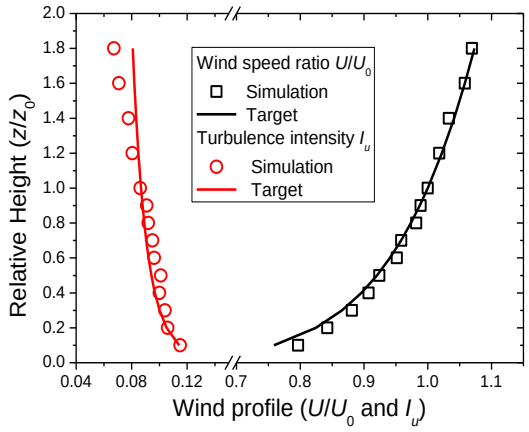

(a) simulation of wind profile

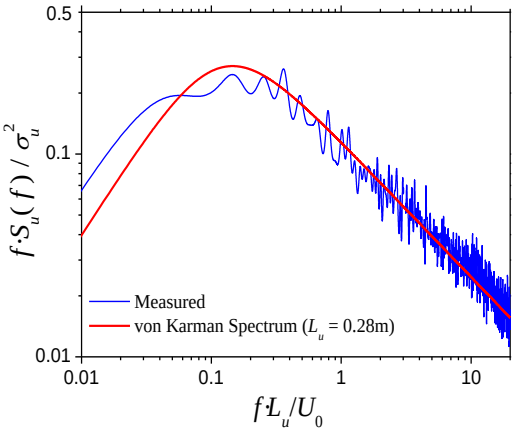

(b) simulation of wind spectrum

Fig. 2 Simulation of costal wind field in the wind tunnel

more flexible.

The present study focuses on the probabilistic and spectral characteristics of fluctuating aerodynamic loads on quayside container cranes in coastal atmospheric boundary layer. The probabilistic and spectral models of aerodynamic wind load are summarized from wind tunnel data. Then, the probabilistic distributions of dynamic wind-induced responses are derived using the probabilistic and spectral models of aerodynamic wind load. Moreover, the results are validated by time domain analysis using wind tunnel data. The presented model can be helpful in determining the unfavorable wind effects in engineering practices.

2 Wind tunnel tests

2.1 Wind field simulation

The wind tunnel tests were carried out in the boundary layer wind tunnel at Tianjin Research Institute for Water Transport Engineering (TIWTE). The open circuit wind tunnel with test section dimension 4.4 m (width) x 2.5 m (height) x 15 m (length) was driven by a 400kW DC motor with rated speed 540r/min.

The approaching flow was assumed to follow type A in Chinese code GB50009-2012, which was a power law wind profile with exponential index α=0.12, representing the costal terrain.

$$U = U_0 \cdot (z/z_0)^{\alpha} \tag{1}$$

$$I_u = I_{u10} \cdot (z/10)^{-\alpha} \tag{2}$$

where U is the mean wind velocity (m/s) at height z(m). U_0 is the mean wind velocity (m/s) at reference height z_0 (m). I_u is the turbulence intensity at height z(m). I_{u10} is the turbulence intensity at 10m height in prototype scale, which is 0.12. The target wind field with geometric scale Λ_L=1:150 was simulated with an arrangement of roughness elements in the wind tunnel.

The fluctuating wind velocity was measured in the center of the test location by a TFI Cobra Probe with sampling frequency 1250 Hz. The comparisons between simulated and target wind profiles are shown in Fig. 2(a), with the reference height z_0 taken as 1m above the wind tunnel floor. The reduced power spectrum of the measured wind velocity at reference height is displayed in Fig. 2(b), which turned out to follow von Karman spectrum.

$$\frac{f \cdot S_u(f)}{\sigma_u^2} = 4 \cdot \frac{f \cdot L_u}{U} \Big/ \left[1 + 70.8 \left(\frac{f \cdot L_u}{U} \right)^2 \right]^{5/6} \tag{3}$$

where f is the frequency (Hz), $S_u(f)$ is the power spectrum of wind velocity at reference height, σ_u^2 is the variance of wind velocity, and L_u is the integral length scale at reference height, which yields 0.28 m at reference height for the present test

2.2 Test models and cases

The tested quayside container crane has a lifting capacity of G=65t, total body mass M=1357t, apex beam height H=80 m (girder height H_1=54.5 m), wheel base B=20.5 m, rail span D=30 m and girder length L_G=67 m and boom length L_B=72 m. Two typical boom positions were considered in the present study. Boom down (with horizontal boom position) is for the service state and boom up (with boom pitch angle 80°) is for out-of-service state. The coordinates X, Y and Z correspond to sea-side, rail-side and vertical directions respectively. The yaw angle θ was clockwise, -90° was for flow coming from sea-side, 0° was for flow coming from rail-side, and 90° was for flow coming from land-side. The crane legs are marked as 1~4. The geometrics of the prototype quayside container crane are shown in Figs. 3(a) and 3(b). According to Figs. 3(a) and (b), positive and negative F_x represent sea- and land-side derailing forces respectively; the absolute value of F_y represents the rail-side sliding force; positive and negative M_y represent sea- and land-side overturning moments respectively; the absolute value of M_x represents the rail-side overturning moment. Hereinafter, cross-rail force F_x and moment M_y are denoted as F_c and M_c; along-rail force F_y and moment $-M_x$ are denoted as F_a and M_a.

The wind tunnel test models were made of aluminum alloy with geometric scale Λ_L=1:150, which are shown in Figs. 3(c) and 3(d). The maximum blockage rate is

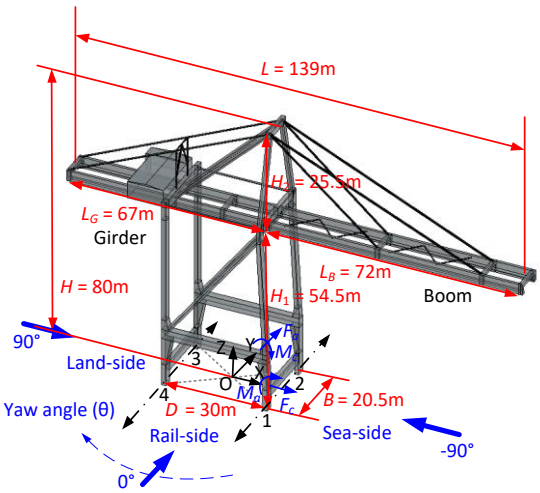

(a) prototype geometrics (boom down)

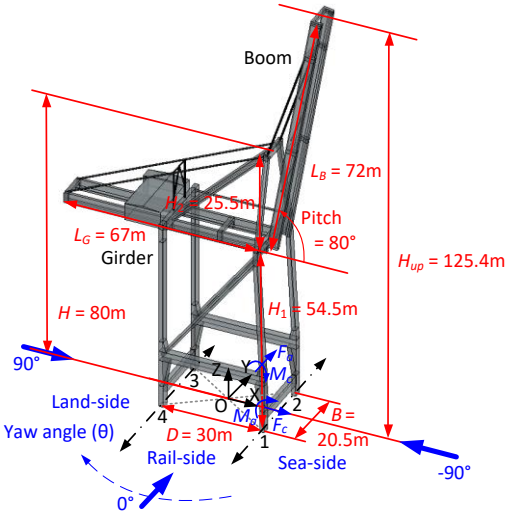

(b) prototype geometrics (boom up)

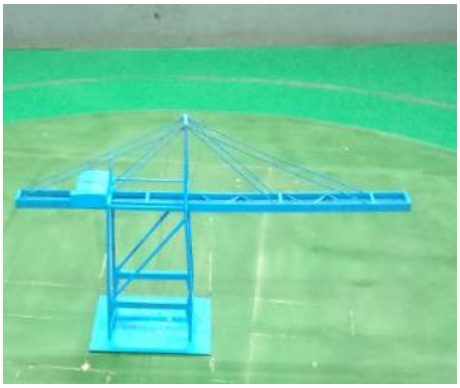

(c) test model (boom down)

(d) test model (boom up)

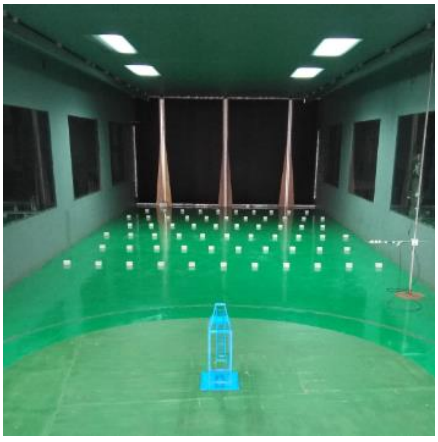

(e) test photo (boom down)

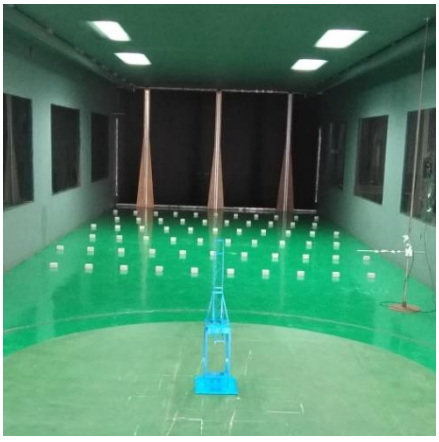

(f) test photo (boom up)

Fig. 3 Wind tunnel test models

approximately 2%.

Each test model was connected to an ATI Delta Series six-component high-frequency force balance (HFFB) installed beneath the center of the turn table of the test section (Figs. 3(e) and 3(f)). By rotating the turn table, cases with yaw angles θ=-90° to 90° (every 15°) were tested. Reported by Kang and Lee(2008), the Reynolds number effect for such structure was not sensitive. The test wind speed was about 10 m/s at apex beam height corresponding to 30 m/s in prototype. Thus, the velocity scale Λ_U was determined as 1:3. According to Strouhal criteria (Eq. (4)), the frequency scale Λ_f was calculated as 50:1, and the time scale Λ_t=1:50.

$$\Lambda_f = 1/\Lambda_t = \Lambda_U / \Lambda_L \tag{4}$$

2.3 Data acquisition and processing

The reference wind velocity U_H was measured by a TFI

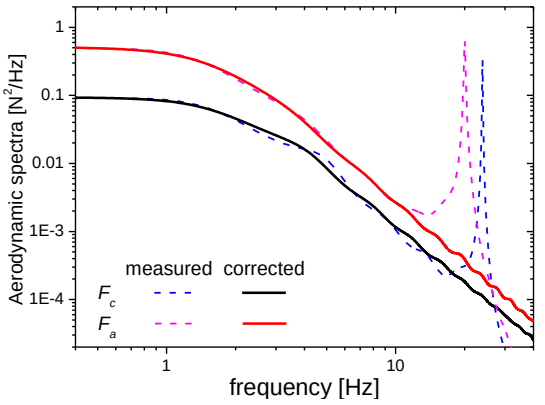

(a) wind force PSD

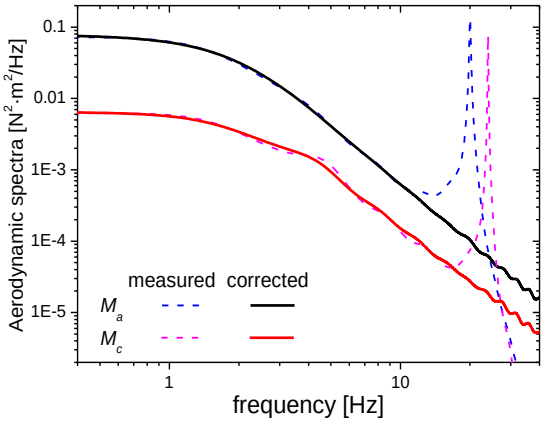

(b) wind moment PSD

Fig. 4 PSDs of the measured and corrected of wind force/moment signals (e.g., boom up, 120° azimuth)

Cobra Probe installed upstream at the apex beam height of the crane model (H=80/150=0.53 m). The aerodynamic wind forces and moments were measured by an ATI Delta Series six-component high-frequency force balance. The sampling frequency of the wind force/moment and velocity was f_s=1000 Hz (corresponding to 20 Hz in prototype), and the sampling duration was T_s=12s (corresponding to 10min in prototype), 5 samples were acquired repeatedly for each case.

The fluctuating aerodynamic wind force/moment signals measured by the HFFB were usually dynamically coupled distorted by the balance-model system (BMS), which requires decoupling and correction. An empirical treatment to the distorted signal is filtering, such as with Butterworth filter (Butterworth, 1930) to remove unwanted spectral peaks. However, the signals in filtered frequency region are heavily distorted. As a compensation, mechanical admittance functions, conventionally estimated by knocking tests, are frequently applied to correct the distortions. Xu *et al*. (2015), introduced a curve fitting approach to correct the uncoupled dynamical distorted signal. In addition, Cui and Caracogia (2016) introduced a coupling coefficient to the mechanical admittance matrix to correct the coupled dynamical HFFB signal. Zhang *et al*. (2018) introduces second-order blind modal identification (SOBI) technique (McNeill 2011, Nagarajaiah and Yang 2015) to decouple the dynamical signal, which uses less assumptions than the approaches mentioned above. Then, the modal parameters are identified by modified Bayesian spectrum density approach (MBSDA, by Au *et al*. 2012) to obtain a more effective correction of distorted HFFB signals. In the present study, the signals corrected by approach proposed by Zhang *et al*. (2018). The results turned out that the combination of SOBI and MBSDA could effectively correct the HFFB signals in a rigid model wind tunnel test. The power spectral density (PSD) of the measured and corrected signals for an arbitrary case were demonstrated in Fig. 4. It was observed that the resonant peaks in the PSDs from measured data induced by the BMS were effectively eliminated through the correction.

The corrected fluctuating aerodynamic wind force/moment, denoted as $F_c(t)$, $F_a(t)$, $M_c(t)$ and $M_a(t)$, were reduced as aerodynamic coefficients $C_{Fc}(t)$, $C_{Fa}(t)$, $C_{Mc}(t)$ and $C_{Ma}(t)$ as Eqs. (5) and (6)

$$C_{Fc}(t_i)=\frac{F_c(t_i)}{0.5\rho U_H^2 BH};\quad C_{Fa}(t_i)=\frac{F_a(t_i)}{0.5\rho U_H^2 DH} \tag{5}$$

$$C_{Mc}(t_i)=\frac{M_c(t_i)}{0.5\rho U_H^2 BH^2};\quad C_{Ma}(t_i)=\frac{M_a(t_i)}{0.5\rho U_H^2 DH^2} \tag{6}$$

where $t_i = i/f_s$ (i = 0, 1, 2, …, N-1) is discrete time. N is the sample length, taken as 1000Hz x 12s=12000 for each sample. ρ is the air density taken as 1.25 kg/m^3.

In order to compare the results with literatures, the resultant force coefficient C_F was defined as Eq. (7).

$$C_F(t_i)=\frac{\sqrt{F_c(t_i)^2+F_a(t_i)^2}}{0.5\rho U_H^2 A} \tag{7}$$

where F_c and F_a are mean aerodynamic forces in cross- and along-rail directions respectively, A is the projected area in XOZ plane.

The mean and root of mean square (RMS) values of the aerodynamic coefficients were calculated by Eq. (8).

$$\bar{C}_{\lambda j}=\mathrm{E}(C_{\lambda j})=\frac{1}{N}\sum_{i=0}^{N-1}C_{\lambda j}(t_i);\quad \tilde{C}_{\lambda j}=\mathrm{SD}(C_{\lambda j})=\sqrt{\frac{1}{N-1}\sum_{i=0}^{N-1}[C_{\lambda j}(t_i)-\bar{C}_{\lambda j}]^2} \tag{8}$$

$\bar{C}_{\lambda j}$ and $\tilde{C}_{\lambda j}$ represent the mean and RMS aerodynamic force/moment coefficient for each component respectively, λ=F or M is for force or moment component, j=a or c for along- or cross- rail direction. E(·) means the mathematical expectation, and SD(·) means the standard deviation. Normalized aerodynamic coefficients were

defined as $C'_{\lambda j}=(C_{\lambda j}-\bar{C}_{\lambda j})/\tilde{C}_{\lambda j}$. High-order statistical moment coefficients (skewness $C_{\lambda j,\mathrm{sk}}$ and kurtosis $C_{\lambda j,\mathrm{ku}}$) of aerodynamic coefficients were calculated by Eq. (9).

$$C_{\lambda j,\mathrm{sk}}=\mathrm{E}(C'^{3}_{\lambda j})=\frac{1}{N}\sum_{i=0}^{N-1}\left[\frac{C_{\lambda j}(t_i)-\bar{C}_{\lambda j}}{\tilde{C}_{\lambda j}}\right]^3;$$
$$C_{\lambda j,\mathrm{ku}}=\mathrm{E}(C'^{4}_{\lambda j})=\frac{1}{N}\sum_{i=0}^{N-1}\left[\frac{C_{\lambda j}(t_i)-\bar{C}_{\lambda j}}{\tilde{C}_{\lambda j}}\right]^4 \quad (9)$$

Besides, the correlation coefficient of the aerodynamic force/moment components between cross- and along- rail directions was calculated by Eq. (10).

$$\rho_{\lambda ca}=\mathrm{E}(C'_{\lambda c}C'_{\lambda a})=\frac{\mathrm{E}(C_{\lambda c}C_{\lambda a})-\mathrm{E}(C_{\lambda c})\mathrm{E}(C_{\lambda a})}{\mathrm{SD}(C_{\lambda c})\cdot\mathrm{SD}(C_{\lambda a})}$$
$$=\frac{\frac{1}{N}\sum_{i=0}^{N-1}C_{\lambda c}(t_i)\cdot C_{\lambda a}(t_i)-\bar{C}_{\lambda c}\cdot\bar{C}_{\lambda a}}{\tilde{C}_{\lambda c}\cdot\tilde{C}_{\lambda a}} \quad (10)$$

where λ, $\eta = F$ or M is for force or moment component.

3 Modelling the fluctuating wind load

3.1 Statistical characteristics and probabilistic model

3.1.1 Data validation

By comparing the data obtained from the present wind tunnel tests with literatures (Huang *et al*. 2007, Kang and Lee 2008, Han and Han 2011), the test was validated. It can be observed from Fig. 5 that the tendencies of mean resultant aerodynamic force results are in good agreement. It was also indicated that as the wind profile index α increases, the wind force coefficients tend to decrease. Because the height of reference velocity was taken at the apex beam, larger wind profile index α indicates lower average mean velocity over the height of crane models. Besides, the aerodynamic forces of boom up position are larger than those of boom down position due to lager upwind area and higher total height.

3.1.2 Statistical characteristics

The mean and RMS aerodynamic force/moment coefficients calculated by Eqs. (4) and (5) are demonstrated in Fig. 6, where the dots indicate the mean values, and the lengths of notches represent the RMS values. It was observed that the tendencies of aerodynamic force and moment with yaw angle are similar. The cross-rail aerodynamic force/moment is almost symmetric with respect to 0°. The corresponding unfavorable yaw angles are ±15° for boom down position and ±30° for boom up position. The along-rail aerodynamic force/moment is almost antisymmetric with respect to 0°. The corresponding unfavorable yaw angles are ±60° for boom down position

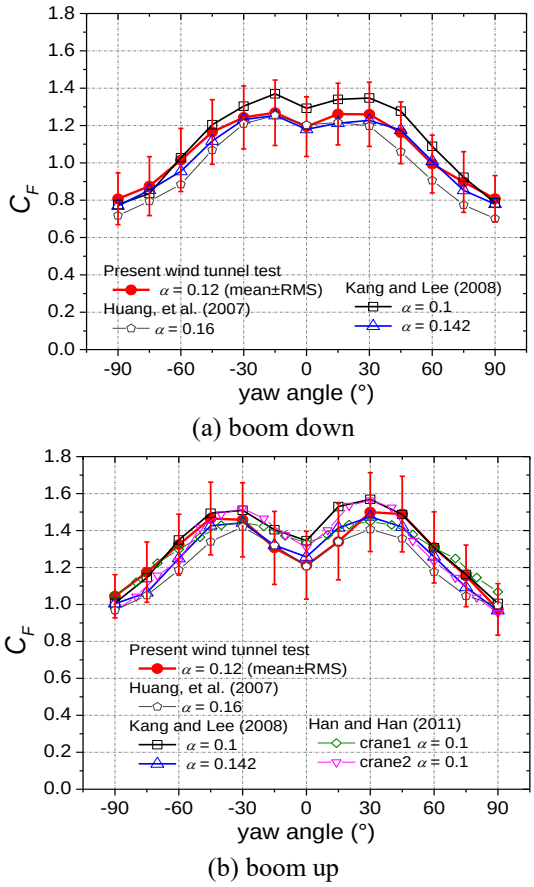

(a) boom down

(b) boom up

Fig. 5 Comparison of drag coefficients of present study with literatures

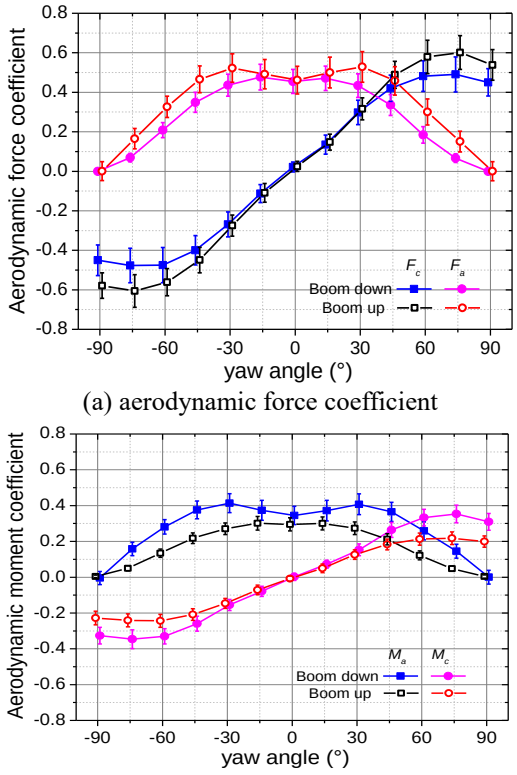

(a) aerodynamic force coefficient

(b) aerodynamic moment coefficient

Fig. 6 Mean and RMS aerodynamic force/moment coefficients (mean ± RMS)

Table 1 Mean and RMS values aerodynamic force/moment coefficients

Boom position	Azimuth (°)	C_{Fc}		C_{Fa}		C_{Mc}		C_{Ma}	
		mean	RMS	mean	RMS	mean	RMS	mean	RMS
Boom up	-90	-0.58	0.065	0.00	0.048	-0.33	0.047	0.00	0.037
	-75	-0.61	0.083	0.17	0.051	-0.35	0.052	0.16	0.038
	-60	-0.56	0.069	0.33	0.054	-0.33	0.043	0.28	0.040
	-45	-0.45	0.065	0.47	0.068	-0.26	0.042	0.38	0.050
	-30	-0.27	0.054	0.52	0.072	-0.15	0.031	0.41	0.053
	-15	-0.11	0.047	0.49	0.074	-0.08	0.028	0.37	0.056
	0	0.03	0.026	0.46	0.070	0.00	0.020	0.35	0.051
	15	0.15	0.041	0.50	0.078	0.07	0.022	0.37	0.058
	30	0.32	0.056	0.53	0.078	0.15	0.033	0.41	0.058
	45	0.49	0.068	0.46	0.072	0.26	0.042	0.37	0.053
	60	0.58	0.085	0.30	0.066	0.33	0.046	0.26	0.050
	75	0.60	0.085	0.15	0.053	0.35	0.049	0.15	0.039
	90	0.54	0.077	0.00	0.048	0.31	0.047	0.00	0.039
Boom down	-90	-0.45	0.077	0.00	0.012	-0.23	0.038	0.00	0.007
	-75	-0.48	0.087	0.07	0.022	-0.24	0.036	0.05	0.014
	-60	-0.47	0.089	0.21	0.038	-0.24	0.036	0.13	0.023
	-45	-0.40	0.074	0.35	0.051	-0.21	0.032	0.22	0.030
	-30	-0.27	0.064	0.44	0.056	-0.15	0.028	0.27	0.033
	-15	-0.11	0.045	0.48	0.065	-0.07	0.027	0.30	0.038
	0	0.02	0.025	0.45	0.061	-0.01	0.014	0.30	0.037
	15	0.14	0.048	0.47	0.062	0.05	0.024	0.30	0.036
	30	0.30	0.062	0.43	0.060	0.13	0.027	0.27	0.036
	45	0.42	0.066	0.34	0.053	0.18	0.030	0.21	0.031
	60	0.48	0.078	0.18	0.042	0.21	0.034	0.12	0.025
	75	0.49	0.089	0.07	0.022	0.22	0.035	0.05	0.014
	90	0.45	0.069	0.00	0.014	0.20	0.032	0.00	0.009

and ±75° for boom up position. It is also indicated from statistical analysis that for such unfavorable cases, the RMS aerodynamic coefficients are usually 12% ~ 15% of the mean aerodynamic coefficients. The data are summarized in Table 1 for engineering reference.

Besides, the coefficients of determination between aerodynamic forces and moments of a certain axis was above 0.97, which indicates that the action height of aerodynamic force in each axis were stable. As the action height of aerodynamic load in j (= a or c) direction h_j can be defined as,

$$\frac{h_j}{H}=\frac{M_j}{F_jH}=\frac{C_{Mj}}{C_{Fj}} \tag{11}$$

The reduced action height h_j/H is obtained by least square estimation of the slope between corresponding aerodynamic moment and force coefficients. The results are shown in Fig. 7. It is concluded that the action height of cross-rail aerodynamic force of boom down case is about half of the height of apex beam. The action heights of along-rail aerodynamic loads are approximately 35% taller than that of the cross-rail aerodynamic loads. The action heights of aerodynamic loads for boom up cranes are approximately 20% taller than those of boom down cranes.

3.1.3 Probabilistic distribution

According to high-order statistical analysis, the skewness of aerodynamic data was within ±0.2, and the kurtosis of aerodynamic data was within 3.0 ± 0.2. The probabilistic distribution functions (PDF) and quantile-quantile plots (QQ plot) of normalized aerodynamic coefficients were shown in Fig. 8. It was observed that the distribution of aerodynamic load fit well with Gaussian distribution.

The correlation coefficients of aerodynamic forces/moments between cross- and along- rail directions ρ_{Fca} and ρ_{Mca} were shown in Fig. 9. It is indicated that the correlation coefficients vary with yaw angle like a sine function. At yaw angle ±45°, the correlation coefficients of aerodynamic loads between the two main axes reach the peaks of approximately ±0.65.

As the statistics and correlations of the fluctuating wind loads on quayside container cranes are studied, the joint probabilistic distribution of aerodynamic force/moment vector can be assumed as 2D Gaussian distribution, written as Eq. (12).

$$f_{C\lambda}(C_{\lambda c},C_{\lambda a})=\frac{1}{2\pi\tilde{C}_{\lambda c}\tilde{C}_{\lambda a}\sqrt{1-\rho_{\lambda ca}^2}}\exp\left[-\frac{C_{\lambda c}'^2-2\rho_{\lambda ca}C_{\lambda c}'C_{\lambda a}'+C_{\lambda a}'^2}{2(1-\rho_{\lambda ca}^2)}\right] \tag{12}$$

According to probabilistic theory,

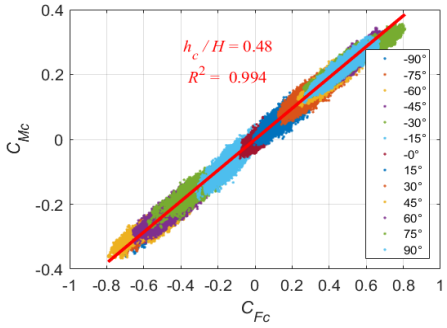

(a) Boom down, cross-rail

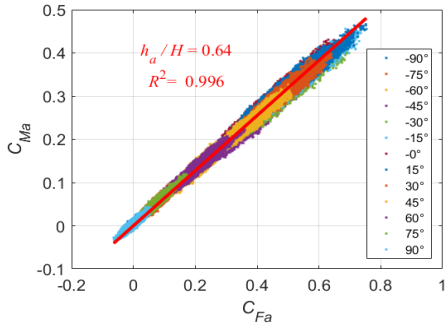

(b) Boom down, along-rail

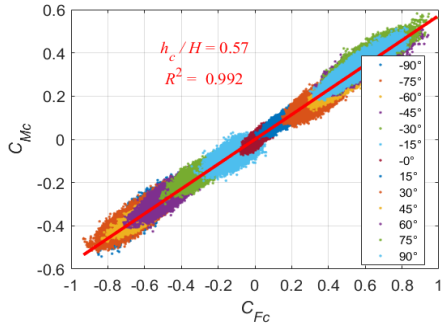

(c) Boom up, cross-rail

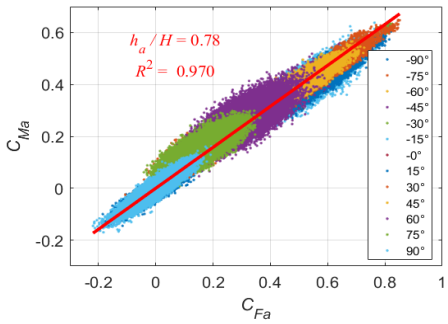

(d) Boom up, along-rail

Fig. 7 Relation between the aerodynamic force and moment coefficients

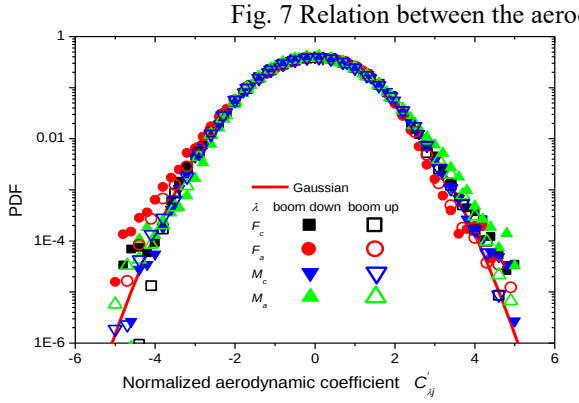

(a) PDF

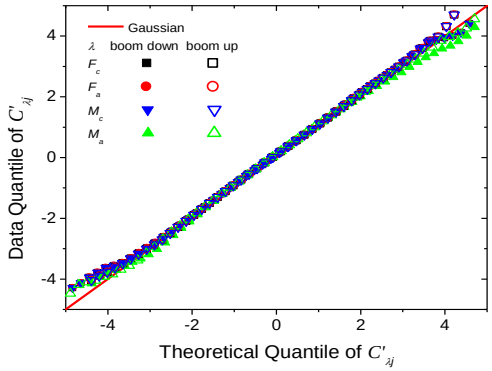

(b) QQ plot

Fig. 8 Probabilistic distributions of the normalized aerodynamic coefficients

$$\chi^2=\frac{C'^2_{\lambda c}-2\rho_{\lambda c,\lambda a}C'_{\lambda c}C'_{\lambda a}+C'^2_{\lambda a}}{1-\rho^2_{\lambda c,\lambda a}}$$

should follow Chi-square distribution with 2 degrees-of-freedom, which is also equivalent to exponential distribution with rate parameter 1/2. Then, the probability p of $(C_{\lambda c}, C_{\lambda a})$ located within the elliptical region $\frac{C'^2_{\lambda c}-2\rho_{\lambda c,\lambda a}C'_{\lambda c}C'_{\lambda a}+C'^2_{\lambda a}}{1-\rho^2_{\lambda c,\lambda a}}<\chi^2_p$ can be determined

$$p=P\left(\frac{C'^2_{\lambda c}-2\rho_{\lambda c,\lambda a}C'_{\lambda c}C'_{\lambda a}+C'^2_{\lambda a}}{1-\rho^2_{\lambda c,\lambda a}}<\chi^2_p\right)=1-\exp\left(-\frac{\chi^2_p}{2}\right) \quad (13)$$

The area of elliptical region with non-exceedance probability p was $-2\ln(1-p)\cdot\pi\tilde{C}_{\lambda c}\tilde{C}_{\lambda a}\sqrt{1-\rho^2_{\lambda ca}}$.

3.2 Spectral characteristics and model

3.2.1 Spectral characteristics

The power spectral density (PSD) functions of aerodynamic loads were estimated by Welch method denoted as $S(f)$. The spectra were reduced with $fS(f)/\sigma^2$, where f is frequency, and σ^2 is variance of corresponding aerodynamic load, which is integration of $S(f)$ over the whole frequency range. The reduced spectra were plotted in double logarithm coordinate with reduced frequency fl/U_H,

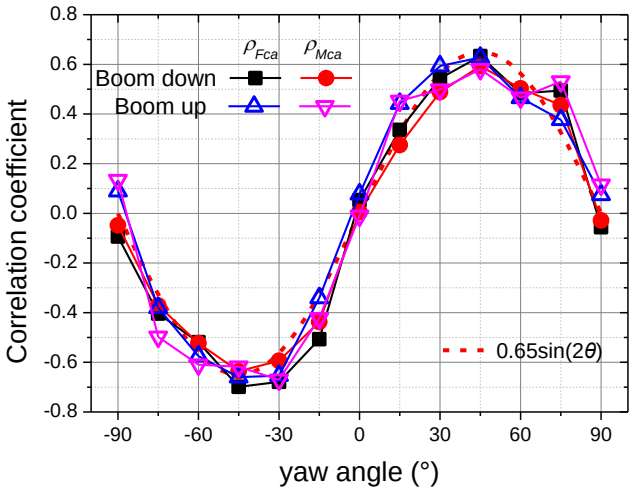

Fig. 9 Correlation coefficients of aerodynamic forces/moments between cross- and along- rail directions

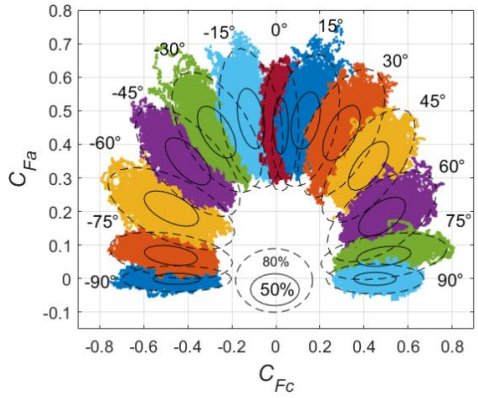

(a) Boom down, aerodynamic force

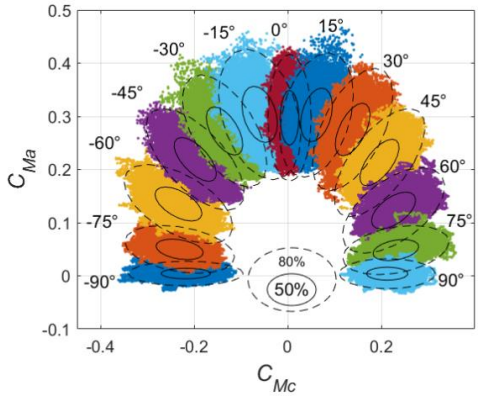

(b) Boom down, aerodynamic moment

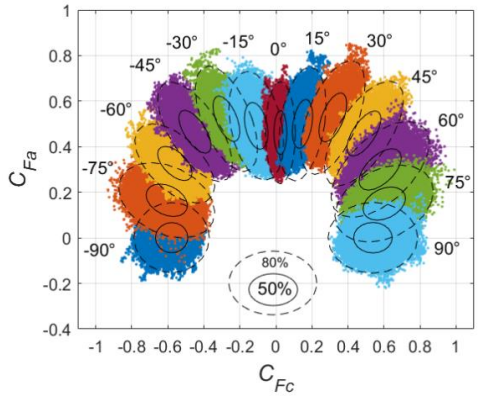

(c) Boom up, aerodynamic force

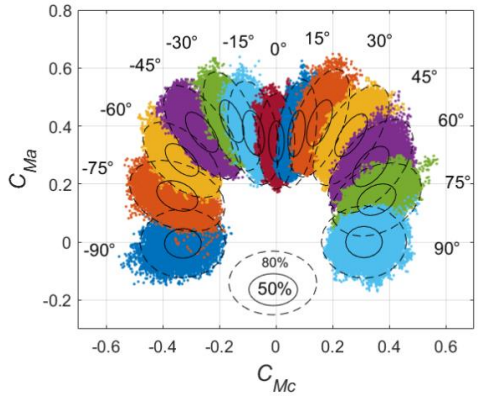

(d) Boom up, aerodynamic moment

Fig. 10 Joint probabilistic distribution of aerodynamic loads

where l is reference length taken as B or D for cross- or along- rail direction respectively.

The reduced power spectral density curves of aerodynamic load under typical yaw angles (0° and ±90°) are displayed in Fig. 11. Furthermore, the spectra for most unfavorable cases were given in Fig. 12. It is observed that the spectral distribution of forces and moments of a certain direction under same yaw angle were similar, which further indicates that the aerodynamic force act in a relatively stable height, thus forming the overturning moments.

3.2.2 Spectral modelling

It was also indicated from Figs. 11 and 12 that the shapes of spectral curves were similar to tri-parameter

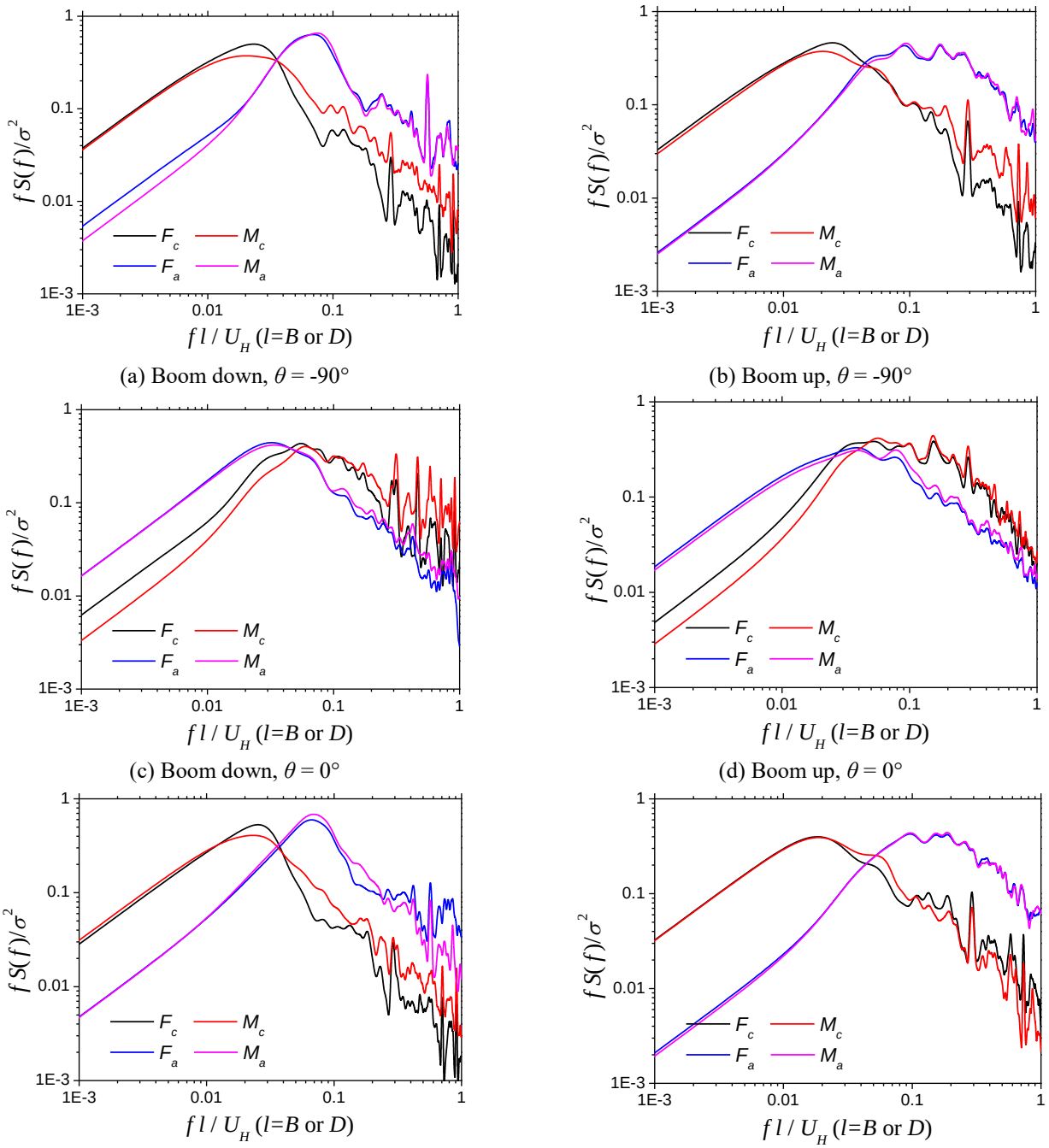

(a) Boom down, θ = -90°

(b) Boom up, θ = -90°

(c) Boom down, θ = 0°

(d) Boom up, θ = 0°

(e) Boom down, θ = 90°

(f) Boom up, θ = 90°

Fig. 11 Reduced power spectral density curves of aerodynamic load under typical yaw angles

model (Su *et al*. 2016). In order to simplify the spectra for the advantage of estimating dynamic responses, filtering approaches (Spanos *et al*. 2017) for the spectra of aerodynamic loads were introduced to the modelling, which was written as Eq. (14).

$$\frac{f \cdot S(f)}{\sigma^2} = \frac{2}{\pi} \cdot \frac{f / f_m}{1+(f / f_m)^2} \tag{14}$$

where f_m is the frequencies of the peaks of reduced aerodynamic load spectra, estimated by f_m= argmax[$fS(f)/\sigma^2$] (argmax is a function that returns the index of maximum, i.e., x_0= argmax[$f(x)$] means $f(x_0)$=max[$f(x)$]). The results of $f_m l/U$ are shown in Fig. 13. It can be observed that the values of reduced f_m are almost symmetric with yaw angle. The values of f_m for boom up cases tend to be higher than boom down cases. For direct yaw angle 0° and ±90°, the cross-wind f_m is much higher than along-wind direction. For oblique flow such as ±45°, the values of f_m for all directions are similar to each other. For the case of most unfavorable aerodynamic loads, reduced f_m seems to be lower than 0.04.

The comparison between the simplified model and spectral curves of all cases are shown in Fig. 14. It isobserved that the reduced spectra for the boom down case

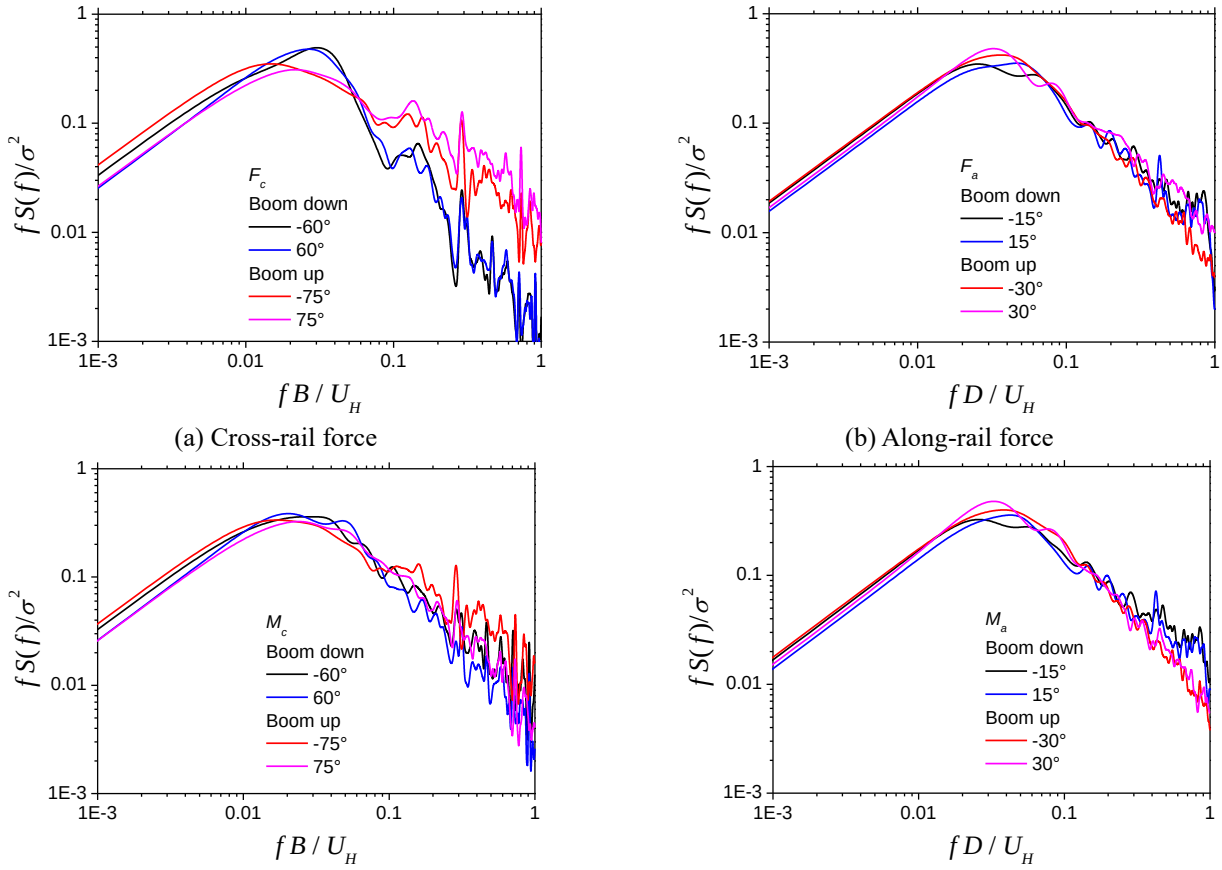

(a) Cross-rail force (b) Along-rail force

(c) Cross-rail moment (d) Along-rail moment

Fig. 12 Reduced power spectral density curves of aerodynamic load under most unfavorable yaw angles

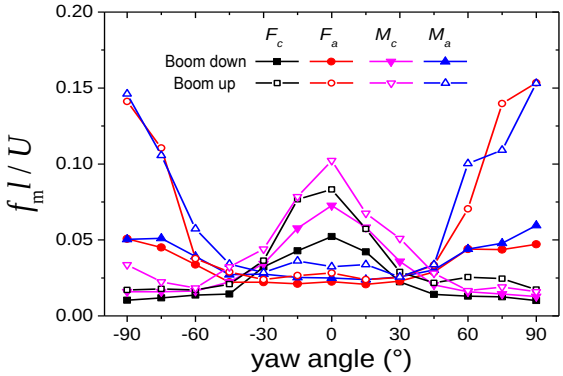

Fig. 13 Reduced frequencies of the peaks of reduced spectra

tend to decay faster than those for boom up case. The model turned out to reflect the overall tendency of the spectral distribution over the frequency.

4 Modelling dynamic wind-induced response

4.1 Theoretical study

4.1.1 Dynamic wind-induced response analysis method

The dynamic wind-induced vibrations of the container crane in cross- and along- rail directions are simplified as a single-degree-of-freedom (SDOF) system with frequency f_{nj} and damping ratio ξ_n. According to stochastic theory, the frequency response function of j (=c or a) axis $H_j(f)$ of the reaction forces is expressed as Eq. (15). The time domain wind-induced dynamic response analysis is carried out with pseudo excitation method (PEM, Lin *et al*, 1994 and 2011; Xu *et al*. 1999), written as Eq. (16).

$$H_j(f)=\frac{1}{-(f/f_{nj})^2+2\xi_n \mathrm{i}(f/f_{nj})+1} \tag{15}$$

$$\begin{aligned} D_{\lambda j}(t_q) &= \\ &\sum_{r=0}^{N-1}\left[\sum_{i=0}^{N-1} C_{\lambda j}(t_i)\cdot\exp(-2\pi \mathrm{i} f_r t_i)\cdot H_j(f_r)\right]\cdot\exp(2\pi \mathrm{i} f_r t_i) \\ &= \sum_{r=0}^{N-1}\left[\sum_{i=0}^{N-1}\frac{C_{\lambda j}(t_i)\cdot\exp(-2\pi \mathrm{i}\, ri/N)\cdot f_{nj}^2}{-f_r^2+2\mathrm{i}\xi_n f_{nj} f_r+f_{nj}^2}\right]\cdot\exp(2\pi \mathrm{i}\, ri/N) \end{aligned} \tag{16}$$

where $\mathrm{i}=\sqrt{-1}$ is imaginary unit. t_i and t_q (i, q = 0, 1, 2, …, N-1) are the discrete time in prototype scale. $f_r = f_s/N$ (r = 0, 1, 2, …, N-1) is the r^{th} discrete frequency. The dynamic wind-induced force/moment responses were reduced as force/moment coefficients like Eqs. (5) and (6), denoted as $D_{\lambda j}$. The statistics of dynamic force/moment responses are

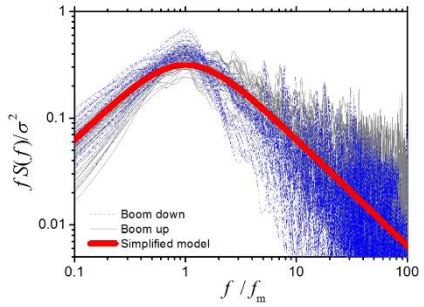

Fig. 14 Simplified model for reduced power spectral density curves of aerodynamic loads

calculated by Eqs. (8) and (9), just replacing the notation of aerodynamic load coefficient C with the response coefficient notation D.

According to structural dynamics, the mean values of $D_{\lambda j}$ equal to those of $C_{\lambda j}$, i. e., $\bar{D}_{\lambda j} = \bar{C}_{\lambda j}$. According to stochastic vibration theorems, the RMS of dynamic force/moment responses can be calculated as Eq. (17).

$$\tilde{D}_{\lambda j} = \tilde{C}_{\lambda j}\sqrt{\int_0^\infty S_{\lambda j}(f)\left|H_j(f)\right|^2 \mathrm{d}f} = \gamma_j \tilde{C}_{\lambda j} \tag{17}$$

where $S_{\lambda j}(f)$ is the normalized (with unit integration) power spectral density function of aerodynamic load component λ_j. γ_j is defined as the dynamic amplification factor. To substitute the spectral model Eq. (14) into Eq. (17), we can obtain the analytic solution of the integration based on Cauchy's residue theorem (Su *et al*. 2018), as Eq. (18).

$$\begin{aligned}\gamma_j &= \sqrt{\int_0^\infty \frac{2}{\pi}\cdot\frac{f_{\mathrm{m}j}}{f^2+f_{\mathrm{m}j}^2}\cdot\frac{f_{\mathrm{n}j}^4}{(f_{\mathrm{n}j}^2-f^2)^2+(2\xi_{\mathrm{n}}f_{\mathrm{n}j}f)^2}\mathrm{d}f} \\ &= \sqrt{1+2\xi_{\mathrm{n}}\frac{f_{\mathrm{m}j}}{f_{\mathrm{n}j}}-\left(1+2\xi_{\mathrm{n}}\frac{f_{\mathrm{n}j}}{f_{\mathrm{m}j}}\right)^{-1}}\end{aligned} \tag{18}$$

where $f_{\mathrm{m}j}$ is the frequency of the peaks of reduced aerodynamic load spectra for j axis. Besides, γ_j can also be solved by Davenport's approximation method (Davenport, 1995), as Eq. (19).

$$\begin{aligned}\gamma_j &= \sqrt{\int_0^\infty S_{\lambda j}(f)\left|H_j(f)\right|^2 \mathrm{d}f} \approx \sqrt{1+\frac{\pi}{4\xi_{\mathrm{n}}}\cdot f_{\mathrm{n}j}S_{\lambda j}(f_{\mathrm{n}j})} \\ &= \sqrt{1+\frac{1}{2\xi_{\mathrm{n}}}\cdot\frac{f_{\mathrm{n}j}f_{\mathrm{m}j}}{f_{\mathrm{n}j}^2+f_{\mathrm{m}j}^2}}\end{aligned} \tag{19}$$

When the structural frequency $f_{\mathrm{n}j}$ is far larger than $f_{\mathrm{m}j}$ (usually $f_{\mathrm{n}j}/f_{\mathrm{m}j} > 5$), the expression can be further simplified as,

$$\gamma_j = \sqrt{1+\frac{1}{2\xi_{\mathrm{n}}}\cdot\frac{f_{\mathrm{m}j}}{f_{\mathrm{n}j}}} \tag{20}$$

The above Eq. (20) can be also used to formulate the simplified equivalent static wind load.

Further, the wind-induced dynamic uplift forces in the legs $\mathbf{N} = \{\mathrm{N_1}\ \mathrm{N_2}\ \mathrm{N_3}\ \mathrm{N_4}\}\mathrm{T}$ can be calculated by,

$$\mathbf{N} = \mathbf{R}\cdot\begin{Bmatrix} D_{Mc} \\ D_{Ma}\end{Bmatrix} = \frac{1}{4}\rho U_H^2 H^2 \tag{21}$$

where $\mathbf{R} = \frac{1}{4}\rho U_H^2 H^2 \begin{bmatrix} B/D & -D/B \\ B/D & D/B \\ -B/D & D/B \\ -B/D & -D/B\end{bmatrix}$ is transfer matrix between moment coefficient vector $\{D_{Mc}, D_{Ma}\}^{\mathrm{T}}$ and the uplift force vector $\mathbf{N}$.

4.1.2 Probabilistic evolution analysis

Based on the aforementioned probabilistic model of aerodynamic loads, the probabilistic evolution of dynamic force/moment response coefficient would be studied in this section.

Firstly, the dynamic force/moment response coefficient $D_{\lambda j}$ is normalized as $D'_{\lambda j} = (D_{\lambda j} - \bar{D}_{\lambda j})/\tilde{D}_{\lambda j}$. Statistically, $\bar{D}_{\lambda j} = \bar{C}_{\lambda j}$, and $\tilde{D}_{\lambda j} = \gamma_j \tilde{C}_{\lambda j}$, thus, we have

$$D_{\lambda j} = \bar{D}_{\lambda j} + \tilde{D}_{\lambda j}\cdot D'_{\lambda j} = \bar{C}_{\lambda j} + \gamma_j \tilde{C}_{\lambda j} D'_{\lambda j} \tag{22}$$

The dynamic response can also be divided the into the mean, background, and resonant components $\bar{D}_{\lambda j}$, $D_{\mathrm{B}\lambda j}$ and $D_{\mathrm{R}\lambda j}$ as Eq. (23).

$$\begin{aligned}D_{\lambda j} &= \bar{D}_{\lambda j} + D_{\mathrm{B}\lambda j} + D_{\mathrm{R}\lambda j} = \bar{C}_{\lambda j} + \tilde{C}_{\lambda j} C'_{\lambda j} + D_{\mathrm{R}\lambda j} \\ &= C_{\lambda j} + D_{\mathrm{R}\lambda j}\end{aligned} \tag{23}$$

According to stochastic vibration theory, the background response is the quasi-static response of aerodynamic fluctuating wind load. Thus, we have $D_{\mathrm{B}\lambda j} = \tilde{C}_{\lambda j} C'_{\lambda j}$. Then, the sum of mean and background response is $\bar{D}_{\lambda j} + D_{\mathrm{B}\lambda j} = C_{\lambda j}$.

As the resonant component was mainly induced by the structure mode in direction j, it is assumed to be dependent on aerodynamic load. Then, we have $\tilde{D}_{\lambda j}^2 = \tilde{C}_{\lambda j}^2 + \tilde{D}_{\mathrm{R}\lambda j}^2$. According to statistical relationship as expressed in Eq. (22), the standard deviation of resonant component yields $\tilde{D}_{\mathrm{R}\lambda j} = \sqrt{\gamma_j^2 - 1}\cdot\tilde{C}_{\lambda j} \approx \sqrt{\frac{\pi}{4\xi_{\mathrm{n}}}\cdot\frac{f_{\mathrm{m}j}}{f_{\mathrm{n}j}}}\cdot\tilde{C}_{\lambda j}$. Assuming the resonant component follows Gaussian distribution as well, the dynamic response tuned out to follow Gaussian distribution.

According to Eq. (23), the resonant response can be expressed as $D_{\mathrm{R}\lambda j} = D_{\lambda j} - C_{\lambda j}$. Then, we have $\tilde{D}_{\mathrm{R}\lambda j}^2 = \tilde{D}_{\lambda j}^2 + \tilde{C}_{\lambda j}^2 - 2\rho_{CDj}\tilde{C}_{\lambda j}\tilde{D}_{\lambda j}$, where ρ_{CDj} is the

correlation coefficient between aerodynamic load and dynamic response. To substitute the aforementioned $\tilde{D}_{\mathrm{R}\lambda j}=\sqrt{\gamma_j^2-1}\cdot\tilde{C}_{\lambda j}$, we have, $\rho_{CDj}=1/\gamma_j$.

The correlation coefficient of the dynamic force/moment response coefficient between cross- and along- rail directions was denoted as $\rho'_{\lambda ca}$, which yields $\rho_{\lambda ca}/\gamma_c\gamma_a$, proved as follows.

$$\begin{aligned}\rho'_{\lambda ca}&=\mathrm{E}\,(D'_{\lambda c}D'_{\lambda a})=\frac{\mathrm{E}\,(D_{\lambda c}D_{\lambda a})-\mathrm{E}\,(D_{\lambda c})\mathrm{E}(D_{\lambda a})}{\mathrm{SD}(D_{\lambda c})\cdot\mathrm{SD}(D_{\lambda a})}\\&=\frac{\mathrm{E}[(C_{\lambda c}+D_{\mathrm{R}\lambda c})(C_{\lambda a}+D_{\mathrm{R}\lambda a})]-\mathrm{E}(C_{\lambda c})\mathrm{E}(C_{\lambda a})}{\gamma_c\mathrm{SD}(C_{\lambda c})\cdot\gamma_a\mathrm{SD}(C_{\lambda a})}\\&=\frac{\mathrm{E}(C_{\lambda c}C_{\lambda a})+\mathrm{E}(D_{\mathrm{R}\lambda c}C_{\lambda a})+\mathrm{E}(C_{\lambda c}D_{\mathrm{R}\lambda a})+\mathrm{E}(D_{\mathrm{R}\lambda c}D_{\mathrm{R}\lambda a})-\mathrm{E}(C_{\lambda c})\mathrm{E}(C_{\lambda a})}{\gamma_c\gamma_a\cdot\mathrm{SD}(C_{\lambda c})\mathrm{SD}(C_{\lambda a})}\end{aligned}\tag{24}$$

$$=\frac{1}{\gamma_c\gamma_a}\cdot\frac{\mathrm{E}(C_{\lambda c}C_{\lambda a})-\mathrm{E}(C_{\lambda c})\mathrm{E}(C_{\lambda a})}{\mathrm{SD}(C_{\lambda c})\mathrm{SD}(C_{\lambda a})}=\frac{\rho_{\lambda ca}}{\gamma_c\gamma_a}$$

where the resonant responses were assumed to be dependent on aerodynamic loads as aforementioned, thus, we have

$$\mathrm{E}(D_{\mathrm{R}\lambda c}C_{\lambda a})=\mathrm{E}(D_{\mathrm{R}\lambda c})\mathrm{E}(C_{\lambda a})=0$$

and

$$\mathrm{E}(C_{\lambda c}D_{\mathrm{R}\lambda a})=\mathrm{E}(C_{\lambda c})\mathrm{E}(D_{\mathrm{R}\lambda a})=0$$

The resonant responses in cross- and along- rail directions were assumed to be dependent because they were induced by different structural modes. Thus we have

$$\mathrm{E}(D_{\mathrm{R}\lambda c}D_{\mathrm{R}\lambda a})=\mathrm{E}(D_{\mathrm{R}\lambda c})\mathrm{E}(D_{\mathrm{R}\lambda a})=0$$

It is also indicted that the covariance of dynamic force/moment response was equivalent to that of aerodynamic force/moment.

After the statistics and correlations of the dynamic force/moment responses are determined, the joint probabilistic distribution of dynamic force/moment response vector can be derived as Eq. (25).

where $D''_{\lambda j}$ is the dynamic force/moment response coefficient normalized by aerodynamic statistics, i. e. $D''_{\lambda j}=(D_{\lambda j}-\bar{C}_{\lambda j})\big/\tilde{C}_{\lambda j}=\gamma_j(D_{\lambda j}-\bar{D}_{\lambda j})\big/\tilde{D}_{\lambda j}=\gamma_j D'_{\lambda j}$. The area of elliptical region with non-exceedance probability p was $-2\ln(1-p)\cdot\pi\tilde{C}_{\lambda c}\tilde{C}_{\lambda a}\sqrt{\gamma_c^2\gamma_a^2-\rho_{\lambda ca}^2}$, which is $\sqrt{\dfrac{\gamma_c^2\gamma_a^2-\rho_{\lambda ca}^2}{1-\rho_{\lambda ca}^2}}$ times aerodynamic loads.

Then, according to Eq. (21), the covariance matrix of wind-induced uplift force can be written as Eq. (26).

$$\begin{aligned}\mathbf{\Sigma_N}&=\mathbf{R}\cdot\begin{bmatrix}\tilde{D}_{Mc}^2 & \rho'_{Mac}\tilde{D}_{Mc}\tilde{D}_{Ma}\\ \rho'_{Mac}\tilde{D}_{Mc}\tilde{D}_{Ma} & \tilde{D}_{Ma}^2\end{bmatrix}\cdot\mathbf{R}^{\mathrm{T}}\\&=\mathbf{R}\cdot\begin{bmatrix}\gamma_c^2\tilde{C}_{Mc}^2 & \rho_{Mac}\tilde{C}_{Mc}\tilde{C}_{Ma}\\ \rho_{Mac}\tilde{C}_{Mc}\tilde{C}_{Ma} & \gamma_a^2\tilde{C}_{Ma}^2\end{bmatrix}\cdot\mathbf{R}^{\mathrm{T}}\end{aligned}\tag{26}$$

After acquiring the mean and RMS values of the dynamic responses, peak responses could be estimated by traditional peak factor approaches.

4.2 Case validation

4.2.1 Finite element model and modal analysis

The finite element (FE) models of the quayside container crane were built with ANSYS. The material was assumed as isotropic steel with density 7850kg/m^3, modulus of elasticity 2.06 x 10^{5}MPa, and Poisson's ratio 0.3. BEAM188 elements with realistic sections were applied to simulate the structural components of the container crane. And MASS21 elements were applied at corresponding nodes to simulate the attached mass of auxiliary facilities (such as machine house, trolley, hoisting, staircase, etc.) on the container crane. The legs of the container cranes were assumed to be anchored at their bases. The FE models of the container crane at boom down and boom up positions were shown in Fig. 15.

The fundamental frequencies of the quayside container crane are obtained through eigenvalue analyses. The results are shown in Fig. 15. The frequency of along-rail mode (f_{na}) was usually lower than that of cross-rail mode (f_{nc}) in both boom down and boom up positions. And the frequencies of corresponding modes for boom up position are lower than boom down position, due to higher total height. The values of frequencies are close to those reported in the literatures (Soderberg *et al*. 2009, Sourav and Samit 2014, Takahashi *et al*. 2016). The damping ratio is assumed as 0.02 for each mode.

4.2.2 Dynamic wind-induced response

The dynamic wind-induced force/moment responses were calculated based on the wind tunnel data with Eqs. (15) and (16). The mean and RMS values of reduced dynamic responses are plotted in Fig. 16. The results of γ_j estimated by the ratio between RMS dynamic response and aerodynamic loads are compared with empirical formula as expressed by Eqs. (18) ~ (20), shown in Fig. 17. It is observed that the simplification presented by Eq. (20) gives better envelope of the results, which is recommended to be applied in the engineering practices.

The comparisons between correlation coefficient results of dynamic responses and theoretical derivation Eq. (24) are shown in Fig. 18. Good agreements are observed, which indicates that the assumptions in 4.1.2 are acceptable, which will be further discussed in the following section 4.3.

The skewness and kurtosis of wind-induced responses were almost within ±0.3 and 3 ± 0.3, which shows less "Gaussian" than those of aerodynamic loads. Nevertheless, the Gaussian assumption seems still acceptable due to itssimplification in calculation. The joint probabilistic distributions of dynamic reduced cross- and along- rail moment responses (estimated by Eq. (25)) and aerodynamic cross- and along- rail moment coefficients (estimated by Eq. (12)) were shown in Fig. 19. It was observed that the results were conformed to theoretical analysis.

The peak responses including dynamic sliding forces, overturning moments, uplift forces of legs estimated from

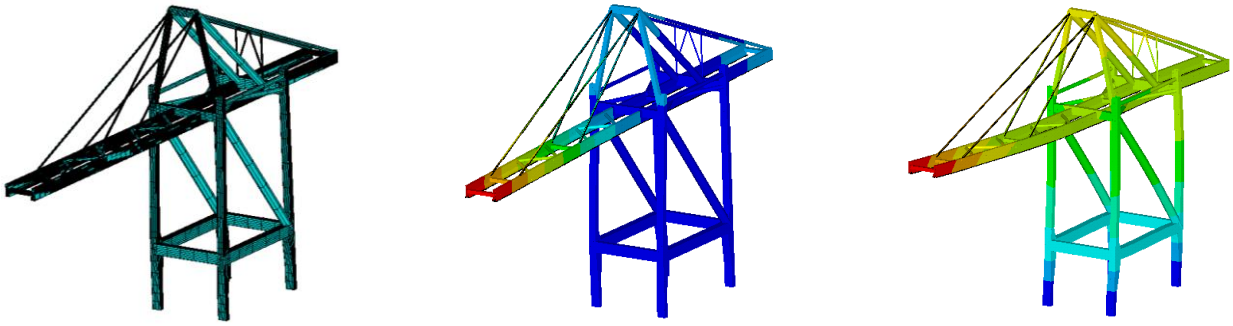

FE model f_{na} = 0.32Hz f_{nc} = 0.77Hz

(a) boom down

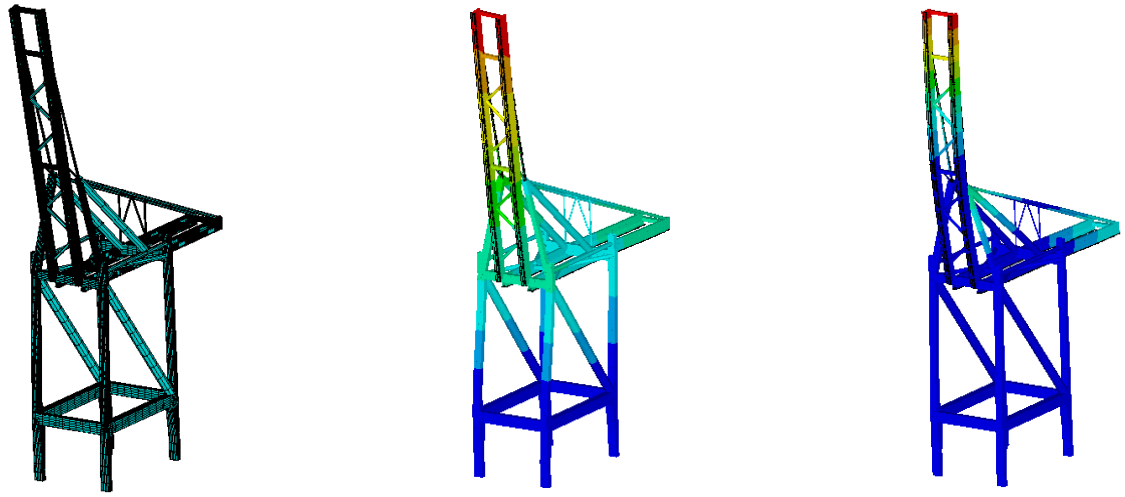

FE model f_{na} = 0.27Hz f_{nc} = 0.39Hz

(b) boom up

Fig. 15 FE models and fundamental modes (at each direction) of the container crane

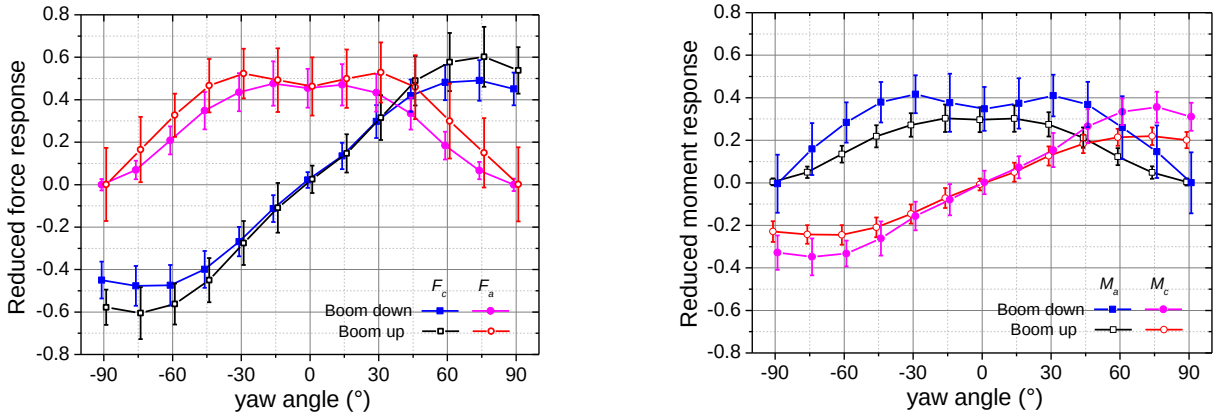

(a) reduced dynamic force response (b) reduced dynamic moment response

Fig. 16 Mean and RMS reduced dynamic force/moment responses

the presented approach were compared to those obtained from time domain analysis (see Fig. 20). The results turned out to be well-agreed, and the presented approach tends to envelope the most unfavorable response.

4.3 Discussion

In section 4.1.2, the resonant responses were assumed as gaussian and independent of each other, then the statistical and correlative relationship between dynamic responses and aerodynamic loads are established. To further check the assumption, the probabilistic distribution and correlation map of $\{D_{Mc}, C_{Mc}, D_{RMc}, D_{Ma}, C_{Ma}, D_{RMa}\}$ are shown in Fig, 21. The diagonal sub-figures are the histograms of the upper triangular sub-figure matrix are theoretical values of correlation of was coefficients.

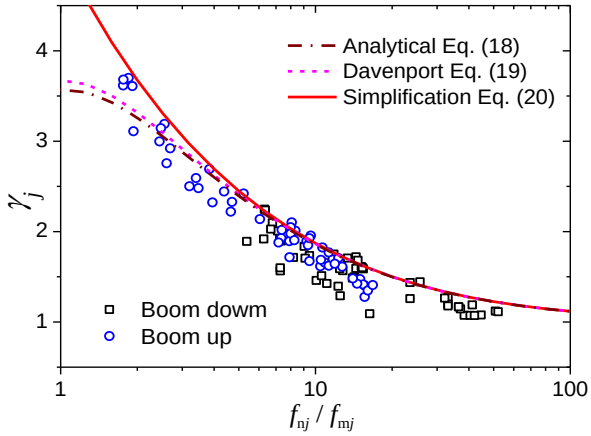

Fig. 17 Comparisons of calculation results and empirical formula for γ_j

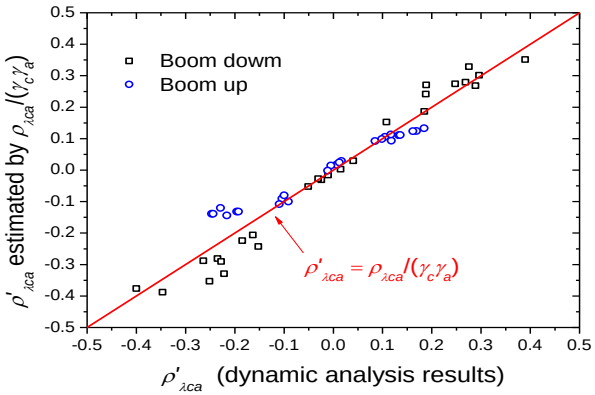

Fig. 18 Comparisons of correlation coefficient results between dynamic analysis and theoretical derivation

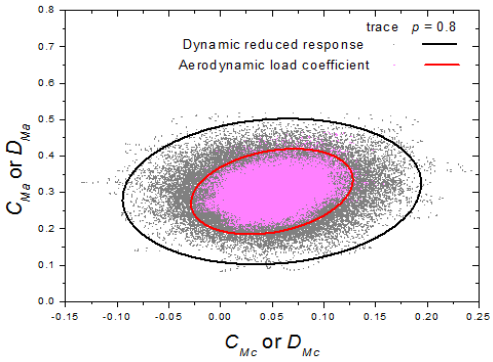

(a) Boom down, θ=15°

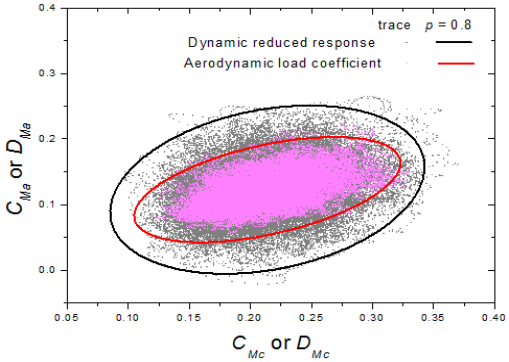

(b) Boom down, θ=60°

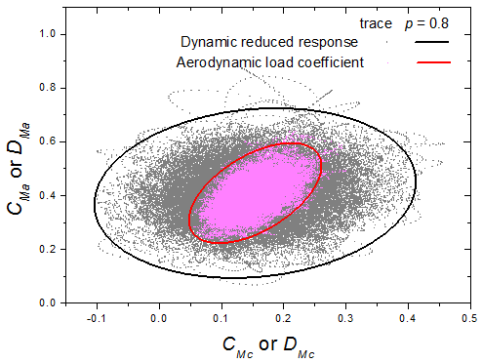

(c) Boom up, θ=30°

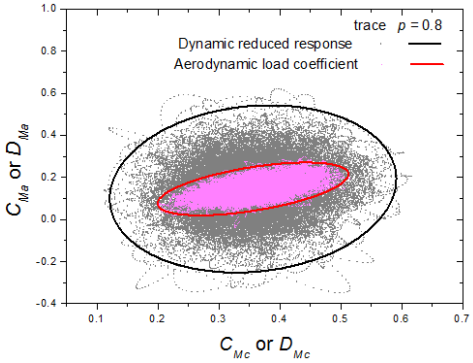

(d) Boom up, θ=75°

Fig. 19 Joint probabilistic distribution of dynamic reduced cross- and along- rail moment response under typical unfavorable yaw angles

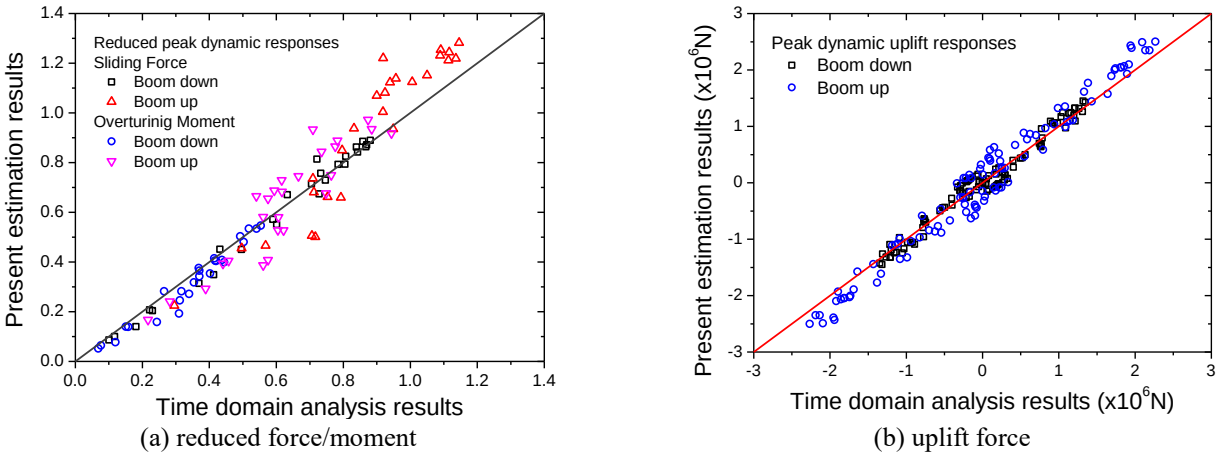

(a) reduced force/moment (b) uplift force

Fig. 20 Comparisons between the peak dynamic responses estimated by present method and time domain analysis

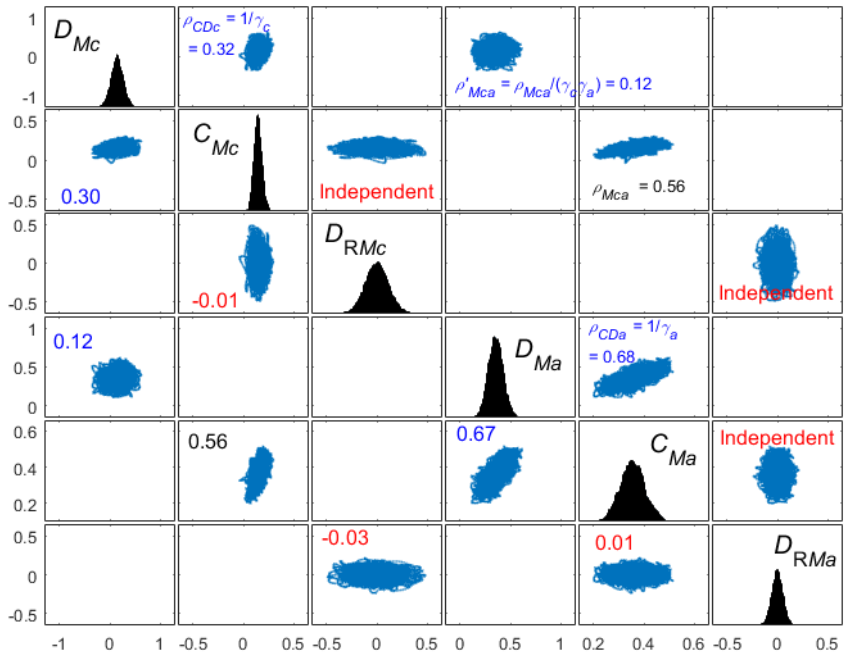

Fig. 21 Probabilistic distribution and correlation map of $\{D_{Mc}, C_{Mc}, D_{RMc}, D_{Ma}, C_{Ma}, D_{RMa}\}$ of a certain unfavorable case (Boom up, $\theta = 75°$)

And the data marked on the lower triangular sub-figure matrix are actual correlation coefficient values estimated by time domain analysis. In the calculation case (Boom up, $\theta = 75°$), the calculation results of γ_c and γ_a were 3.14 and 1.47 respectively, and the correlation coefficient of aerodynamic moments $\rho_{Mca} = 0.56$. According to the theoretical analysis in section 4.1.2, ρ_{CDc}, ρ_{CDa} and ρ'_{Mca} should be 0.32, 0.68 and 0.12 respectively, which are close to time domain analysis results 0.30, 0.67
and 0.12. The reason why these results agreed well might contribute to the conformation of independent assumptions. The correlation coefficients of $\{C_{Mc}, D_{RMc}\}$, $\{C_{Ma}, D_{RMa}\}$ and $\{D_{RMc}, D_{RMa}\}$ are observed to be close to zero. Moreover, according to statistical analysis of all cases, such correlation coefficients were within ±0.05, which indicated that the independent assumption be acceptable.

However, it should also be addressed that if the structural frequencies f_{nc} and f_{na} are too close, there might be coupling effects of resonant responses $\{D_{RMc}, D_{RMa}\}$. Then, D_{RMc} and D_{RMa} are somehow dependent of each other. Then the correlation relationship Eq. (24) should be modified considering the correlation between D_{RMc} and D_{RMa}. Nevertheless, for structures such as container cranes, the stiffness of cross- and along- rail axes are quite different, leading to different axis frequencies. The derivation of probabilistic evolution in this paper can also be applied in the HFFB tests for wind-excited first mode dominated structures such as high-rise structures.

5. Conclusions

In the present research, the aerodynamic load characteristics on quayside container cranes were studied based on wind tunnel tests. Moreover, the characteristics of

dynamic wind-induced responses were studied theoretically and validated numerically. The following concluding remarks were drawn.

• The fluctuating aerodynamic loads obtained from wind tunnel tests seem to follow Gaussian distribution. The most unfavorable azimuth was oblique. And the correlation coefficients between cross- and along- rail axis variate with yaw angle as a sine function.

• The simplified spectral model of fluctuating aerodynamic load was established, which was expressed as a characteristic frequency f_m varies with boom position and yaw angle. The model can be used to simplify the estimation of dynamic responses.

• The dynamic amplification factor γ_j denoted as the ratio between the RMS values of dynamic wind-induced force/moment responses and aerodynamic loads can be simplified as $\sqrt{1+\frac{1}{2\xi_n}\cdot\frac{f_{mj}}{f_{nj}}}$, which could be used to further establish the probabilistic evolution from aerodynamic load and dynamic response.

• The dynamic responses of quayside container cranes approximately follow Gaussian distribution, with RMS amplified by γ_j and correlation coefficient reduced by $1/\gamma_c\gamma_a$. The correlation coefficient between corresponding dynamic response and aerodynamic load component should be $1/\gamma_j$.

• The last conclusion about the correlative relationship between dynamic response and aerodynamic load was based on a series of independent assumptions between background and resonant responses. Usually, the background and resonant responses were independent of each other. When the structural frequencies of two axes were too close, the resonant responses were not independent of each other, which require detailed analysis. However, such situation seems less likely to happen on the quayside container cranes. Thus, using the presented approach, the estimation of dynamic sliding force, overturning moment and uplift responses agree well with results of time domain analysis.

• The present research is for a single stand container crane. However, the quayside container cranes located in the container terminals are usually arranged in line, which might lead to interference effects on the aerodynamic wind loads. The mean wind load might be reduced, whereas the RMS wind load might be amplified. Further investigations can be carried out in detail via the analysis framework presented in this paper.

Acknowledgements

This research was supported by the China National Key R&D Program (Grant No. 2017YFE0130700), Tianjin Municipal Natural Science Foundation (Grant No. 19JCQNJC06700), Tianjin Transportation Science and Technology Development Plan Project (Grant No. 2019B-09), and the Fundamental Research Funds for the Central Public Welfare Research Institutes (Grant Nos. Tks190204 and Tks2020).

References

Au, S.K., Zhang, F.L. and To, P. (2012), "Field observations on modal properties of two tall buildings under strong wind", *J. Wind Eng. Ind. Aerod.*, **101**, 12-23, https://doi.org/10.1016/j.jweia.2011.12.002.

Butterworth, S. (1930), "On the theory of filter amplifiers", *Wireless Engineer*, **7**(6), 536-541.

Chinese Standards. (2012), Load Code for the Design of Building Structures, GB 50009, Beijing: China Architecture & Building Press.

Cui, W. and Caracoglia, L. (2016), "Physics-based method for the removal of spurious resonant frequencies in high-frequency force balance tests", *J. Struct. Eng.*, **142**(2), 04015129. https://doi.org/10.1061/(asce)st.1943-541x.0001414.

Davenport, A.G. (1995), "How can we simplify and generalize wind loads?", *J. Wind Eng. Ind. Aerod.*, **54**(94), 657-669. https://doi.org/10.1016/0167-6105(94)00079-S.

Ding, J. and Chen, X. (2014), "Assessment of methods for extreme value analysis of non-gaussian wind effects with short-term time history samples", *Eng. Struct.*, **80**, 75-88. https://doi.org/10.1016/j.engstruct.2014.08.041.

Gu, M., Huang, P. and Wang, Y.J. (2008), "Numerical simulation of mean wind loads on a container crane and its comparison with experimental results", *J. Tongji Univ.*, **36**(8), 1024-1027.

Han, D.S. and Han, G.J. (2011), "Force coefficient at each support point of a container crane according to the wind direction", Int. *J. Precis. Eng. Manuf.*, **12**(6), 1059-1064. https://doi.org/10.1007/s12541-011-0141-5.

Huang, P., Wang, Y.J. and Gu, M. (2007), "Experimental research on mean wind loads of a quayside container crane", *J. Tongji Univ.* **35**(10), 1384-1389. https://doi.org/10.1016/S1672-6529(07)60007-9.

Kang, J.H. and Lee, S.J. (2008), "Experimental study of wind load on a container crane located in a uniform flow and atmospheric boundary layers", *Eng. Struct.*, **30**(7), 1913-1921. https://doi.org/10.1016/j.engstruct.2007.12.013.

Lee, S.J. and Kang, J.H. (2008), "Wind load on a container crane located in atmospheric boundary layers", *J. Wind Eng. Ind. Aerod.*, **96**(2), 193-208. https://doi.org/10.1016/j.jweia.2007.04.003.

Lin, J.H., Zhang Y.H. and Zhao, Y. (2011), "Pseudo excitation method and some recent developments", *Proc. Eng.*, **14**, 2453-2458. https://doi.org/10.1016/j.proeng.2011.07.308.

Lin, J.H., Zhang, W.S. and Li, J.J. (1994), "Structural responses to arbitrarily coherent stationary random excitations", *Comput. Struct.*, **50**(5), 629-633. https://doi.org/10.1016/0045-7949(94)90422-7.

McCarthy, P. and Vazifdar, F. (2004), "Securing cranes for storm wind: uncertainties and recommendations", *In Ports 2004: Port Development in the Changing World*, Houston, U.S.A.

McCarthy, P., Jordan, M., Lee, K. and Werner, S. (2007), "Increasing hurricane winds dockside crane retrofit recommendations", *ASCE Ports 2007 conference*, San Diego. U.S.A.

McCarthy, P., Soderberg, E. and Dix, A. (2009), "Wind damage to dockside cranes: recent failures and recommendations", *TCLEE 2009 Conference*, Oakland, U.S.A.

McNeill, S.I. (2011), "An analytic formulation for blind modal identification", *J. Vib. Control*, **18**(14), 2111-2121. https://doi.org/10.1177/1077546311429146.

Nagarajaiah, S. and Yang, Y. (2015), "Blind modal identification

of output only non-proportionally -damped structures by time-frequency complex independent component analysis", *Smart Struct. Syst*., **15**(1), 81-97. https://doi.org/10.12989/sss.2015.15.1.081.

Qingdao Port. (2018), Qingdao Port Resumed Normal Production after a Wind Gust Accident. http://www.chineseport.cn/bencandy.php?fid=49&id=274151.

Soderberg, E., Hsieh, J. and Dix, A. (2009), "Seismic guidelines for container cranes", *TCLEE 2009 Conference*, Oakland, U.S.A.

Sourav, G. and Samit R.C. (2014), "Vulnerability assessment of container cranes under stochastic wind loading", *Struct. Infrastruct. Eng*., **10**(12), 1511-1530. https://doi.org/10.1080/15732479.2013.834943.

Spanos, P.D., Sun, Y. and Su, N. (2017), "Advantages of filter approaches for the determination of wind-induced response of large-span roof structures", *J. Eng. Mech*., **143**(9), 04017066. https://doi.org/10.1061/(ASCE)EM.1943-7889.0001261.

Su, N., Cao, Z. and Wu, Y. (2018), "Fast frequency-domain algorithm for estimating the dynamic wind-induced response of large-span roofs based on cauchy's residue theorem", *Int. J. Struct, Stab. Dyn*., **18**(2), 1850037. https://doi.org/10.1142/S0219455418500372.

Su, N., Sun, Y., Wu, Y. and Shen, S. (2016). "Three-parameter auto-spectral model of wind pressure for wind-induced response analysis on large-span roofs", *J. Wind Eng. Ind. Aerod*., **158**, 139-153. https://doi.org/10.1016/j.jweia.2016.09.013.

Sun, Z., Hou, N. and Xiang, H. (2009), "Safety and serviceability assessment for high-rise tower crane to turbulent winds", *Front. Archit. Civ. Eng. China*, **3**(1), 18-24. https://doi.org/10.1007/s11709-009-0009-2.

Takahashi, K., Abe, M. and Fujino, T. (2016), "Runaway characteristics of gantry cranes for container handling by wind gust", *Mech. Eng. J*., **3**(2), 15-00679, 1-16. https://doi.org/10.1299/mej.15-00679.

Xu, A., Xie, Z., Gu, M. and Wu, J. (2015), "A new method for dynamic parameters identification of a model-balance system in high-frequency force-balance wind tunnel tests", *J. Vib. Eng*., **17**(5), 2609-2623. https://www.jvejournals.com/article/15900/pdf.

Xu, Y.L., Zhang, W.S., Ko, J.M. and Lin, J.H. (1999), "Pseudo-excitation method for vibration analysis of wind-excited structures", *J. Wind Eng. Ind. Aerod*., **83**(1-3), 443-454. https://doi.org/10.1016/S0167-6105(99)00092-6.

Zhang, L.L., Xie, Z.N. and Yu, X.F. (2018), "Method for decoupling and correction of dynamical signals in high-frequency force balance tests", *J. Struct. Eng*., **144**(12), 04018216. https://doi.org/10.1061/(ASCE)ST.1943-541X.0002205.

AD